ACS OMEGA

http://pubs.acs.org/journal/acsodf

Article

Confined Crystallization and Melting Behaviors of 3-Pentadecylphenol in Anodic Alumina Oxide Nanopores

Yongdong Liu, Yonghong Wu, Jianqi Yao, Jiajie Yin, Jing Lu, Jie Mao, Min Yao,* and Faliang Luo*

Cite This: *ACS Omega* 2021, 6, 18235−18247

Read Online

ACCESS | Metrics & More | Article Recommendations

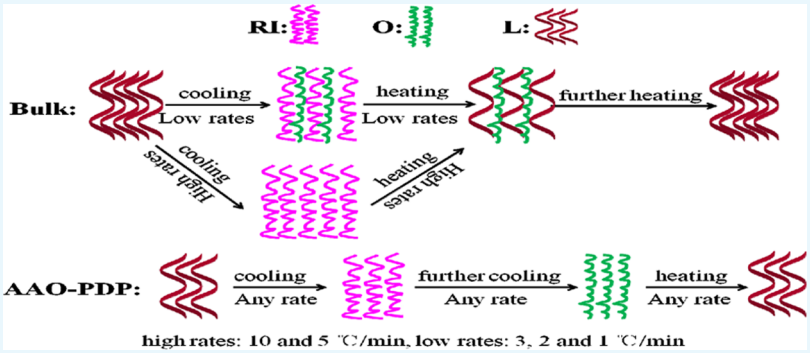

ABSTRACT: To explore the effects of end groups on the confined crystallization of an alkyl chain, 3-pentadecylphenol (PDP) was infiltrated into the anodic aluminum oxide template (AAO) to investigate the melting and crystallization behaviors of PDP in a nanoconfined environment. Wide-angle X-ray diffraction (WAXD) found that the solid−solid phase transition of PDP occurred under confined conditions, and the absence of the (00L) reflections indicated that the stacking of the end groups of the alkyl chain layered structure was seriously disturbed. Thermal analysis (TG) showed that the thermal stability of the confined samples decreased due to the confinement effect, and the introduction of end groups made the confinement effect more obvious. Differential scanning calorimeter (DSC) results well reflected the space−time equivalence in the PDP crystallization processes, i.e., the solid−solid phase transition can be achieved by reducing the cooling rate or confining PDP in the nanometer space. Compared with C_{15}, the introduction of the end groups with a phenol ring led to the disappearance of the solid−solid phase transition of an alkyl chain at high cooling rates. In the confined environment, the introduction of the end groups with a phenol ring caused the melting double peaks of the alkyl chain to become a single melting peak, and it also caused the disappearance of the surface freezing monolayer for alkyl chains. Through the analysis of crystallinity, it was found that AAO-PDP was more sensitive to AAO pore size changes than AAO-C_{15}, the X_c of AAO-PDP had a good linear relationship with the pore size d, but the X_c of the AAO-C_{15} had a nonlinear relationship with the pore size d. Attenuated total reflection (ATR)-IR proved that in the confined environment, the order of the alkyl chain decreased and the degree of chain distortion increased.

1. INTRODUCTION

In the last two decades, with the development of nanotechnology, great attention has been paid to the space-confined phase transition, which could slow down the solid−solid phase transition and separate the processes of crystal growth and nucleation.[1] According to the geometry of the space, it can be divided into one-dimensional,[2,3] two-dimensional,[4−8] and three-dimensional[9−12] confined environment. In these confined systems, changes in the crystalline structure and microscopic morphology cause the physical properties of the polymer to deviate significantly from the bulk, thereby affecting its processing and application performance.[13] From a purely crystallographic point of view, the confined space provides an ideal model, which offers a new perspective for understanding some basic issues of polymer crystal nucleation and growth.[1,14,15] Meanwhile, for crystalline polymers, nucleation mechanism, crystal structure, and dynamic characteristics in the nanoconfined space are different from those of bulk materials,[13,16−19] which can exhibit a series of unique properties in nanoscale and are widely used in membrane, fuel cell, and other fields.[20−22] Aluminum oxide template (AAO) template is an inorganic template prepared by the electrochemical method, which is simple to prepare, with a

Received: April 21, 2021
Accepted: June 28, 2021
Published: July 8, 2021

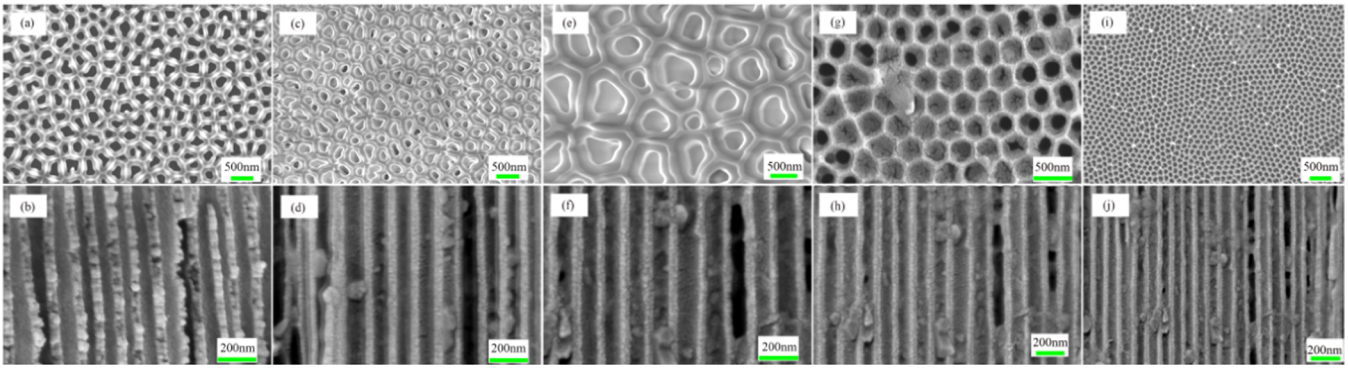

Figure 1. SEM micrographs of (a), (b) surface and cross section of pristine AAO template with the diameter of 250 nm. (c), (d) Surface and cross section of 250 nm AAO-PDP, respectively. (e), (f) Surface and cross section of 450 nm AAO-PDP, respectively. (g), (h) Surface and cross section of 180 nm AAO-PDP, respectively. (i), (j) Surface and cross section of 90 nm AAO-PDP, respectively.

pore diameter from 10 nm to several hundred nanometers, pore depth from several nanometers to several hundred microns,[23] uniform size, high mechanical strength, and good thermal stability;[20,24] so, it is widely used to study the confined crystallization of polymers.[16,24−26]

However, due to the complex crystallization process of high-molecular-weight polymers, molecular-level understanding of its microscopic mechanism is still a challenge.[27] Normal alkanes (*n*-alkanes C_nH_{2n+2}, abbreviated as C_n) have a linear chain molecular structure, which is the basic component of organic, biological, and polymer systems.[10,27−30] Therefore, C_n are usually used as simple models to reveal the crystallization properties of polymer systems by studying their melting and crystallization behaviors under confined conditions.[30−40] For example, by observing the phase transition behaviors of C_n in a confined environment, researchers could infer the nucleation mechanism, crystal structure, and dynamic properties of the polymers at the nanometer scale.[1,3,9,10] However, polymers often have certain end groups due to the addition of terminators or other reasons in the polymerization process, which greatly affect their own crystallization and properties.[41−46] For example, González-Fernández et al. prepared azide-terminated poly(ethylene glycol) (PEGs).[47] The presence of azide end groups caused PEG to form defects in the crystallization, and the size of the crystal was also reduced, resulting in a decrease in the melting temperature of PEG. Therefore, the linear AAO-C_n model maybe cannot well reflect a series of crystallization changes of end-group-functionalized polymers in nanospace. Therefore, the crystallization and melting behaviors of the alkyl chain with end groups in a confined environment may be more similar to that of confined polymers. In this paper, 3-pentadecylphenol (PDP)[48] with a phenol ring end groups was selected to replace *n*-alkanes, and the melting crystallization behaviors of PDP in a nanoconfined environment was studied to provide a more reasonable model for the confined crystallization of end-group polymers.

2. RESULTS AND DISCUSSION

2.1. Morphological Characterization by Scanning Electron Microscopy (SEM). Figure 1a,b shows the surface and cross-sectional SEM micrographs of an AAO template with a pore size of 250 nm before PDP infiltration, respectively. Figure 1c−j are surface and cross-sectional SEM micrographs of the 250, 450, 180, and 90 nm AAO-PDP, respectively. It can be clearly observed from Figure 1 that the pores of AAO are uniformly distributed, and the inner diameter of these pores are basically the same and completely isolated from each other. After PDP infiltration, every nanopore was nearly filled with PDP.

2.2. Wide-Angle X-ray Diffraction (WAXD). Figure 2 shows WAXD diffraction patterns for PDP and AAO-PDP. As

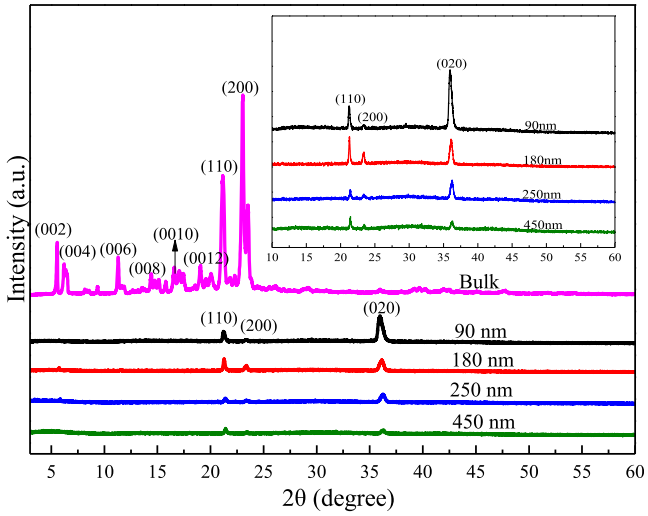

Figure 2. WAXD patterns of bulk PDP and AAO-PDP. The inner illustration on the top right corner is the WAXD patterns of only AAO-PDP samples.

can be seen from the patterns, the diffraction peaks of bulk PDP were more complex. There were not only diffraction peaks of the (110) and (200) crystal planes at 2θ = 21.3 and 23.4° but also diffraction peaks of the (002), (004), (008), (0010), and (0012) crystal planes. The diffraction curves of AAO-PDP were relatively simple. Besides the diffraction peaks at 2θ = 21.3 and 23.4°, a new diffraction peak appeared near 36.3°. This is similar to the diffraction peaks of odd-numbered alkanes in the confined space;[49] the diffraction peaks near 36.3° are the special diffraction corresponding to the (020) crystal plane of the low-temperature ordered orthorhombic phase *Pbcm* (referred as O phase),[50] and the peaks near 21.3 and 23.4° are the special diffraction for the (110) and (200) crystal planes of the rotator phase face-centered orthorhombic *Fmmm* (RI).[51] It can be seen that under the WAXD test conditions described herein, the PDP had only a single RI crystal form, while AAO-PDP had both RI and O crystal forms, i.e., the PDP underwent a phase separation under confined

https://doi.org/10.1021/acsomega.1c02112
ACS Omega 2021, 6, 18235−18247

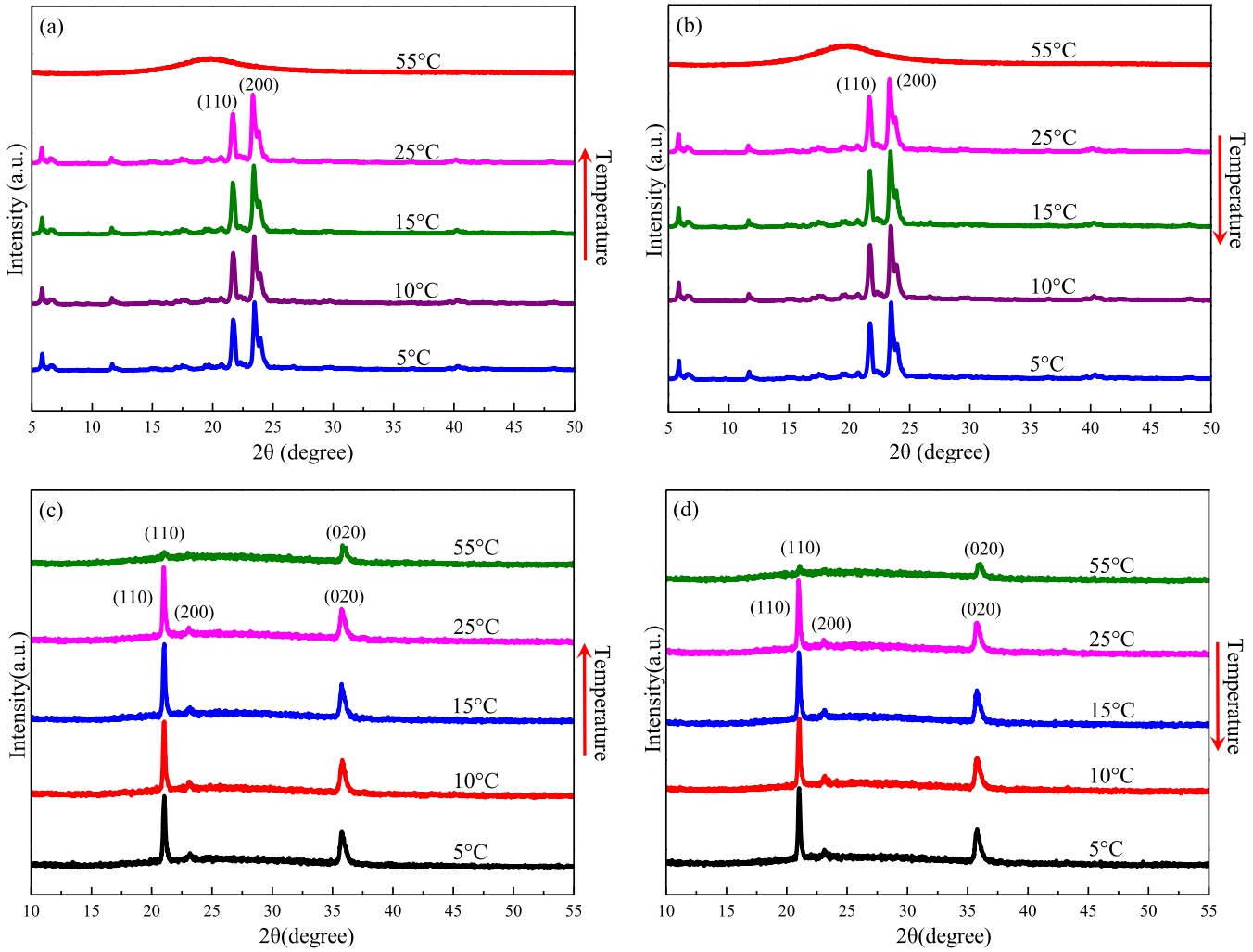

Figure 3. In situ WAXS patterns of (a) heating and (b) cooling processes of bulk PDP, in situ WAXS patterns of (c) heating and (d) cooling processes of 250 nm AAO-PDP. Cooling and heating rates: 2 °C/min.

conditions. At the same time, for AAO-PDP, the RI phase diffraction peaks (00L) disappeared, indicating that the stacking of the end groups of the alkyl chain layered structure was seriously disturbed, or geometric constraints inhibited the longitudinal expansion of the molecular chain. It can be clearly seen from the inner illustration of Figure 2 that the intensity of the O phase diffraction peak (020) gradually increased with the decrease in the confinement space size, indicating that the stronger the confinement was, the more favorable the solid−solid transition was.

To further observe the solid−solid phase before and after confined PDP, in situ WAXS measurements were performed on bulk PDP and 250 nm AAO-PDP. As shown in Figure 3a,b, it can be seen that bulk PDP was a liquid phase at 55 °C, and the diffraction peaks corresponding to the (110) and (200) crystal planes of the RI phase appear as the temperature decreases. There was no diffraction peak corresponding to the O phase in the heating and cooling processes of bulk PDP. However, for a 250 nm AAO-PDP ((Figure 3 c,d), the diffraction peaks corresponding to the (110) crystal plane of the RI phase and the (020) crystal plane of the O phase appeared at 55 °C, the (200) crystal plane of the RI phase also appeared at 25 °C, and the intensity of each diffraction peak at other temperatures was obviously higher than that at 55 °C. This is similar to the change of *n*-hexadecane confined in microcapsules,[27] indicating that the confined environment is conducive to the solid−solid transition.

2.3. Differential Scanning Calorimeter (DSC) Analysis. DSC scans of bulk PDP, AAO-PDP, bulk C_{15}, and AAO-C_{15} samples are shown in Figure 4. During the cooling process (Figure 4a), bulk PDP had an obvious exothermic peak at 24.6 °C. However, the 450 nm AAO-PDP crystallization peak appeared to the obvious trail at the same cooling rate. With a further decrease in the AAO pore size, the single crystal peak changed into double crystal peaks. For example, the crystal peaks of 90 nm AAO-PDP appeared at 6.02 and 14.56 °C, indicating that the PDP underwent a solid−solid phase transition in the confined space (enlarged view in Figure 4a). According to WAXD results, the crystal form corresponding to the crystal peak of bulk PDP was the rotator phase RI, the low-temperature crystal form of AAO-PDP was the O phase, and the high-temperature crystal form of AAO-PDP was the RI phase. It can be seen from Figure 4a that the crystallization temperature T_c^R (about 14.53 °C) of RI phase AAO-PDP samples with different pore sizes was approximately the same, which was about 10 °C lower than that of bulk PDP (24.63 °C). The crystallization temperatures (T_c^O) of 450, 250, 180, and 90 nm AAO-PDP were 12.06, 10.45, 8.88, and 6.02 °C,

https://doi.org/10.1021/acsomega.1c02112
ACS Omega 2021, 6, 18235−18247

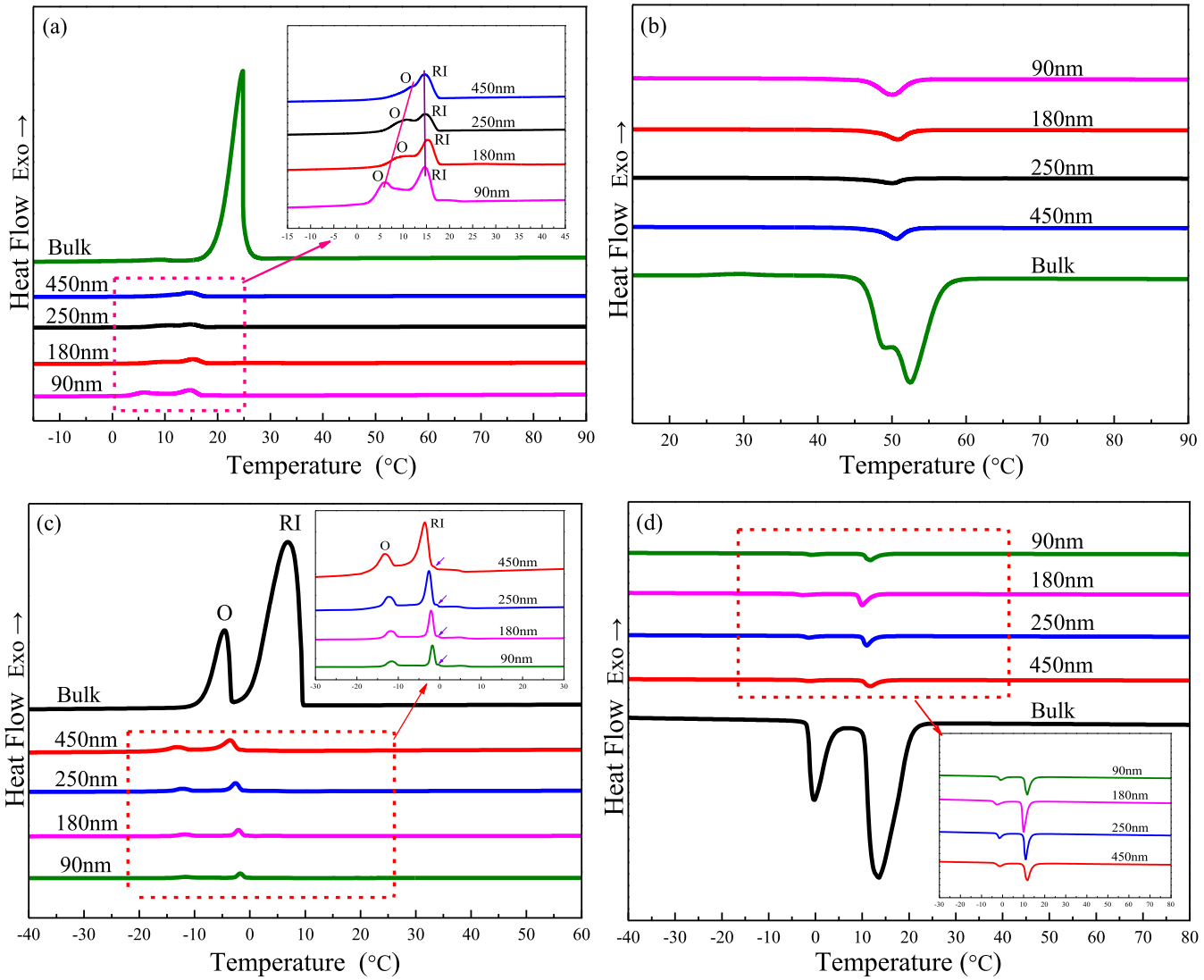

Figure 4. DSC cooling (a) and (b) heating curves of bulk and AAO-PDP samples. DSC cooling (c) and heating (d) curves of the bulk C_{15} and AAO-C_{15} samples. The illustration on the top right corner of a,c are the enlarged view in the dashed box. The illustration on the bottom right corner of d is the enlarged view in the dashed box. Cooling and heating rates: 10 °C/min.

respectively. It can be seen that the T_c^O of AAO-PDP decreased gradually with the decrease in the AAO pore size, which indicated that the smaller the confined geometry, the more obvious the crystallization confinement was. Figure 4c shows the crystallization curves of bulk C_{15} and 450 nm AAO-C_{15}. It can be seen that both bulk C_{15} and confined C_{15} exhibited obvious solid−solid phase transitions during the crystallization process. In addition, the exothermic peak corresponding to the surface freezing monolayer of C_{15} appeared on the 450 nm AAO-C_{15} cooling curve (Figure 4c inset). For *n*-alkanes with a chain length from n = 15 to 50, the surface freezing phenomenon in micro−nanospace has become a consensus.[52] The crystallization of PDP mainly depended on the movement of pentadecyl chain, so the crystallization of PDP was similar to that of *n*-pentadecane, but there were still some differences. Comparing the cooling curves of bulk PDP and bulk C_{15} in Figure 4a,c, we found that the solid−solid phase transition of the alkyl chain disappeared with the introduction of the end groups with a phenol ring. At the same time, the exothermic peak of the surface freezing monolayer of the alkyl chain disappeared due to the introduction of end groups with a phenol ring in the confined environment, which indicated that the end groups had a great influence on the crystallization of the alkyl chain. The confinement effects of AAO nanopores consist of finite-size effect[53] and interfacial effect,[54] so the confined samples can be nucleated at the pore wall (surface nucleation) or within the nanopore volume. Therefore, the volume and polarity of the end groups have a great influence on the movement of the alkyl chain. The strong finite-size effect of the bulky phenol ring in the AAO nanopores led to the weakening of the mobility of the alkyl chain. At the same time, the introduction of phenol ring improved the affinity between the confined alkyl chain and the AAO wall, which affected the movement of the alkyl chain in the nanopore to a certain extent.

Figure 4b shows the DSC heating curves of bulk PDP and the AAO-PDP samples. Bulk PDP showed partially overlapping melting double peaks on the DSC curve, while AAO-PDP showed a single melting peak. The melting temperatures (T_m) of 450, 250, 180, and 90 nm AAO-PDP were 49.93, 50.21, 50.77, and 49.76 °C, respectively. The values T_m of the AAO-PDP samples were approximately the same, which was

https://doi.org/10.1021/acsomega.1c02112
ACS Omega 2021, 6, 18235−18247

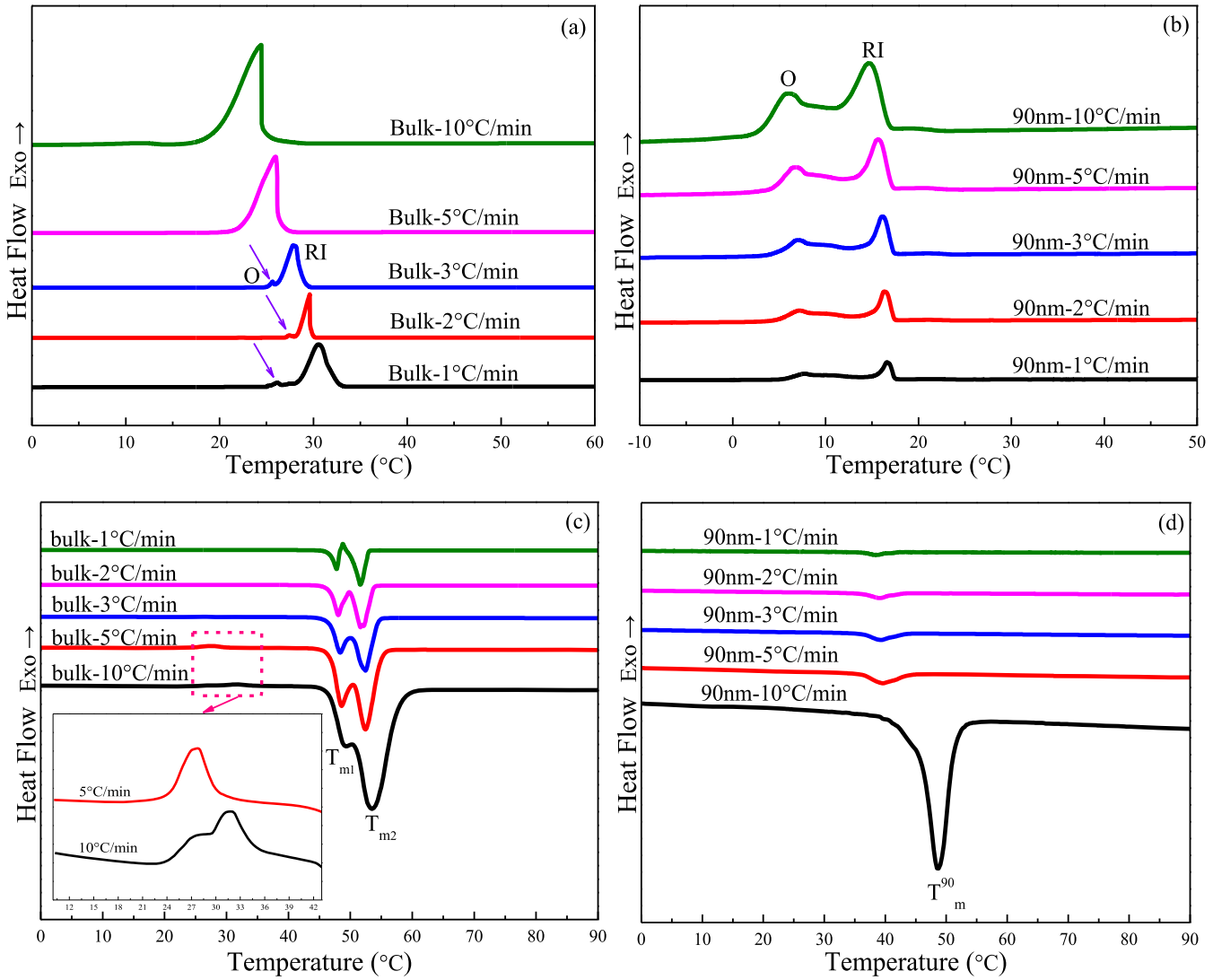

Figure 5. DSC cooling curves of bulk PDP (a) and AAO-PDP samples (b) at different cooling rates. DSC heating curves of bulk PDP (c) and AAO-PDP samples (d) at different heating rates. The cooling and heating rates were 10, 5, 3, 2, and 1 °C/min, respectively. The inserted figure on the bottom left corner of (c) is the cold crystallization peaks of bulk PDP during the heating process at the rate of 5 and 10 °C/min.

independent of the nanopore sizes, indicating that there was only one crystal type in AAO-PDP when the crystallization was completed, and the stability and grain size of the crystal were basically unchanged. However, bulk PDP showed partially overlapping double melting peaks at 49.26 and 53.49 °C, which is very common in the melting processes of semicrystalline polymers.[55] This phenomenon proved that the crystallization of PDP is more similar to that of semicrystalline polymers, so the simulation of the confined crystallization of semicrystalline polymers by PDP is more realistic than that of *n*-alkanes. Figure 4d shows the melting curves of bulk C_{15} and 450 nm AAO-C_{15}. Both bulk C_{15} and AAO-C_{15} showed two melting peaks with a temperature difference of about 13 °C, while there was only a partially overlapping melting peak in bulk PDP (Figure 4b). Also, AAO-PDP always showed only one melting peak, which indicated that the introduction of end groups also had a great influence on the melting behaviors of alkyl chains. The reasons for the double melting peaks are that two crystal structures in the crystallization process, and different morphologies in the crystallization process (such as the thickness, distribution, integrity, or stability of the lamellae), or the influence of melting and recrystallization (during the recrystallization process, defects are embedded in the crystal grains, and the defects melt first), etc.[56−58]

To evaluate the melting and crystallization behaviors of the AAO-PDP samples more clearly, the DSC measurements were performed at different melting and cooling rates of 10, 5, 3, 2, and 1 °C/min. For bulk PDP, only one phase transition emerged during the cooling process (Figure 5a) when the cooling rates were 10 and 5 °C/min, which was related to the phase transition between the RI phase and the liquid phase. However, when the cooling rates changed to 3, 2, and 1 °C/min, it can be observed that there was an extra small sharp exothermic peak in bulk PDP, indicating that the two phase transitions occurred at the low-speed cooling rates. One of them corresponded to the process in which the isotropic liquid transformed into the metastable phase RI, the other corresponded to the process in which the metastable phase RI transformed into the stable orthorhombic phase O. For the AAO-PDP samples, as shown in Figures 5b and 6, two exothermic peaks were detected during all of the cooling processes, corresponding to the transformation of the isotropic

https://doi.org/10.1021/acsomega.1c02112
ACS Omega 2021, 6, 18235−18247

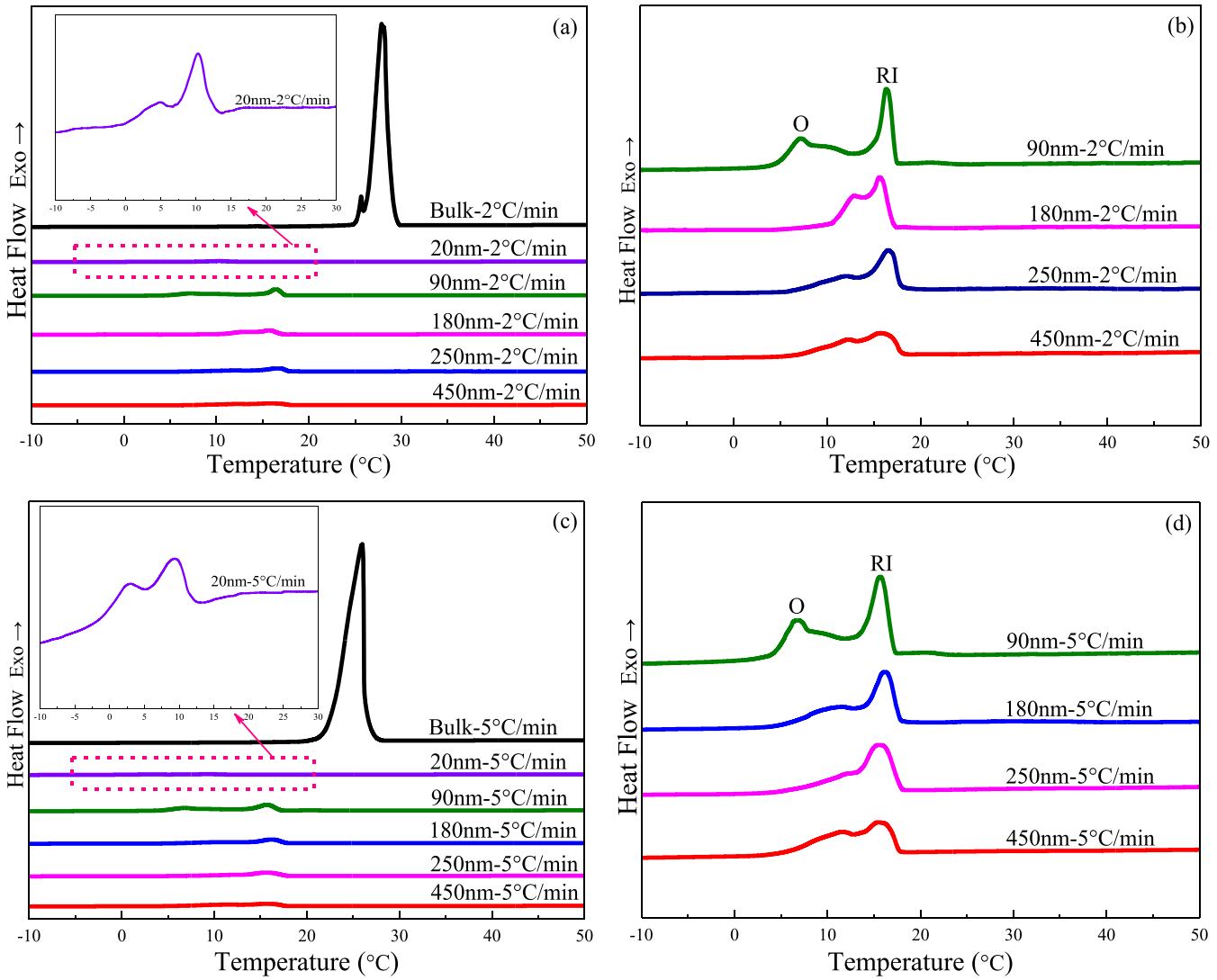

Figure 6. DSC cooling curves (a), (c) of bulk PDP and AAO-PDP samples, respectively, and (b), (d) only AAO-PDP samples (cooling rates were 2 and 5 °C/min). The inserted figures on the top left corner of (a, c) are the cooling curves of 20 nm AAO-PDP.

liquid into the metastable phase RI and the transformation of the metastable phase RI into the stable orthorhombic phase O, respectively. Compared with the new exothermic peaks of bulk PDP at the low cooling rates, the two exothermic peaks of AAO-PDP were obvious at any cooling rates.

As shown in Figure 5c, at all selected heating rates, the melting double peaks can be observed during the heating processes of bulk PDP. Also, as the heating rate decreased, the overlapping melting double peaks gradually became two independent endothermic peaks. It can be confirmed that when the corresponding cooling crystallization was completed, bulk PDP had two different crystal forms,[59] and the melting temperatures of the two crystals were different, resulting in melting double peaks. In other words, the metastable phase with imperfect crystallization formed the low-temperature melting peak, while the stable phase with perfect crystallization formed the high-temperature melting peak.[60] The low-temperature melting peak (T_{m1}) corresponded to the metastable RI phase, and the high-temperature melting peak (T_{m2}) corresponded to the low-temperature ordered phase O. From Figures 5c and 7c, it can be clearly observed that bulk PDP had a small cold crystallization peak during the heating process at the rates of 5 and 10 °C/min. The appearance of a cold crystallization peak also proved that the crystal growth of bulk PDP was imperfect in the process of rapid cooling crystallization. For the AAO-PDP samples (as shown in Figures 5d and 7b,d), only a single melting peak (corresponding to the low-temperature ordered phase O) was observed at different heating rates, indicating that there was only one crystal form at the end of the crystallization process. From the above comparison, it can be concluded that the phase transition processes of bulk PDP and AAO-PDP reflected a certain space−time equivalence, i.e., the phase transitions of PDP can be achieved by reducing the cooling rate or confining PDP in the nanometer space.

As shown in Table 1, the supercooling temperature $\Delta T_{R\to O}$ ($\Delta T_{R\to O} = T_c^R - T_c^O$) between the RI→O transformation of AAO-PDP was about 9 °C and that between the RI→O transformation of bulk PDP was 2−4.5 °C. The higher degree of supercooling temperature made the crystalline transformation of AAO-PDP more thorough than that of bulk PDP. The metastable phase RI of AAO-PDP completely transformed into the stable phase O, while bulk PDP only partially transformed the metastable phase RI into the stable

https://doi.org/10.1021/acsomega.1c02112
ACS Omega 2021, 6, 18235−18247

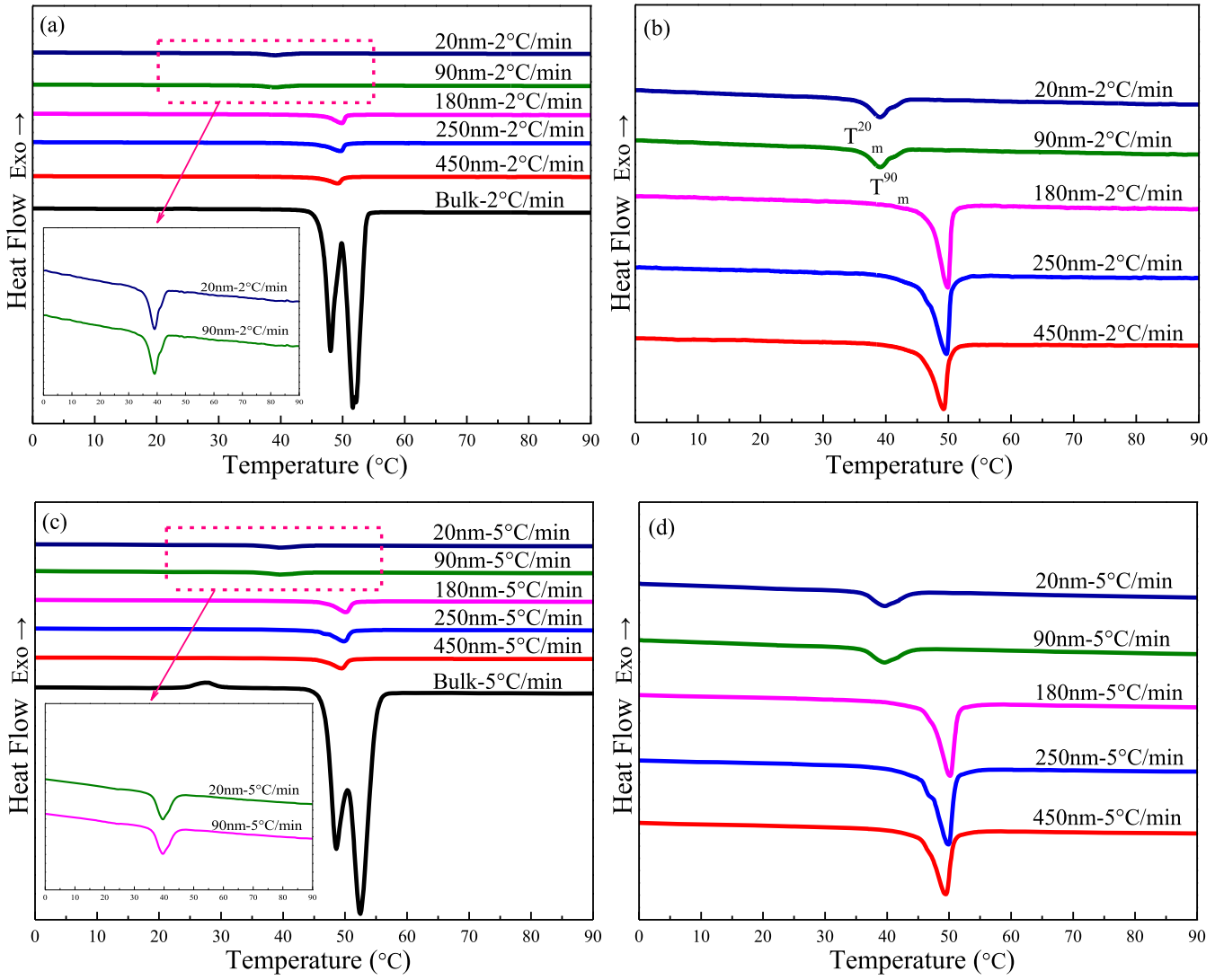

Figure 7. Heating thermograms of (a), (c) bulk and AAO-PDP samples, respectively, and (b), (d) only AAO-PDP samples, respectively (heating rates are 2 and 5 °C/min, respectively).

Table 1. Crystallization, Melting Temperature, and Supercooling of Bulk and AAO-PDP at Different Heating and Cooling Rates

		T_c^R/°C	T_c^O/°C	T_{m1}/°C	T_{m2}/°C	$\Delta T_{R\to O}$/°C
bulk 90 nm	3 °C/min	27.90	25.64	48.60	52.28	2.26
	2 °C/min	29.58	27.26	48.15	51.83	2.36
	1 °C/min	30.58	26.14	47.66	51.73	4.44
	3 °C/min	16.18	6.88		39.41	9.30
	2 °C/min	16.40	7.12		39.24	9.28
	1 °C/min	16.70	7.62		38.75	9.08

phase O. This can be evidenced by the fact that bulk PDP had a double melting peak and AAO-PDP had only a single melting peak.

It should be noted that when the heating rate was 10 °C/min, the melting points of AAO-PDP with different pore sizes were basically the same (Figure 4b). However, when the heating rate decreased, the melting point of 90 nm AAO-PDP (T_m^{90}) reduced significantly (Figure 4d), which was about 10 °C lower than that of the heating process at 10 °C/min. This phenomenon may be caused by the thermal overshoot of PDP during rapid heating in the nanometer confined environment. Also, as shown in Figure 7, when the heating rate decreased, the T_m^{90} was about 10 °C lower than other size-confined PDPs. To eliminate accidental errors, we infiltrated the PDP into a smaller space (20 nm). It can be seen from Figure 7 that the melting point of 20 nm AAO-PDP (T_m^{20}) was similar to T_m^{90} at the heating rates of 5 and 2 °C/min and T_m^{20} and T_m^{90} were about 10 °C lower than the T_m of AAO-PDP of other sizes. This indicated that when the confinement effect strengthened, the stacking interference of the end groups ($-CH_3$ and phenol ring) of the PDP layered structure also became stronger. The diameter of the PDP molecular chain is close to the nanometer level and the phenol ring part is relatively large.[61] Therefore, when the size of the confined

https://doi.org/10.1021/acsomega.1c02112
ACS Omega 2021, 6, 18235−18247

space is less than 100 nm, the molecular chain accumulation is greatly disturbed, which leads to the reduction of molecular freedom and a sharp decline in crystal stability.

Through the above analysis, the movement of the molecular chain of PDP during the melting and crystallization processes can be obtained. The movements of the molecular chain of bulk PDP and AAO-PDP during the cooling and subsequent melting processes are shown in Figure 8; the chain movement of bulk PDP varied with the cooling and heating rates, while the molecular chain movement of AAO-PDP remained unchanged at any cooling and heating rates.

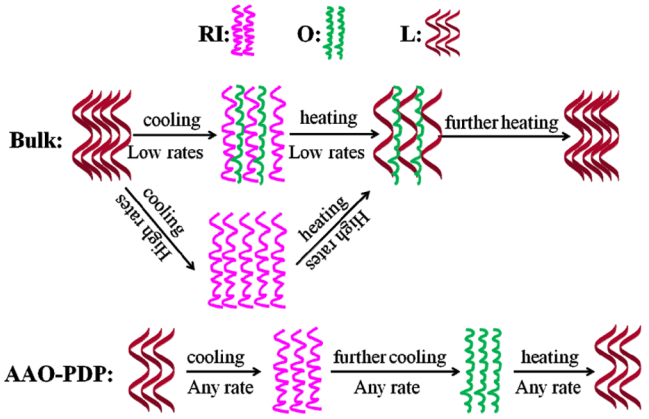

Figure 8. Movement of the molecular chain of bulk PDP and AAO-PDP during the cooling and subsequent melting processes (high rates: 10 and 5 °C/min; low rates: 3, 2, and 1 °C/min).

2.4. TG Analysis. According to the TG analysis (Figure 9a), bulk PDP began to decompose at 314.6 °C, while 450, 250, 180, and 90 nm AAO-PDP began to decompose at 245.9, 218.7, 199.5, and 196.9 °C, respectively. It can be seen from Figure 9b that bulk PDP reached the maximum thermal decomposition rate at 347.1 °C, and 450, 250, 180, and 90 nm AAO-PDP reached the maximum thermal decomposition rates at 278.4, 251.2, 237.5, and 228.5 °C, respectively. As shown in Figure 9c,d, bulk C_{15} began to decompose at 129.3 °C and reached the maximum decomposition rate at 193.2 °C. However, the AAO-C_{15} sample began to decompose at about 40 °C and reached the maximum thermal decomposition rate at about 150 °C. By comparing the thermal decomposition processes of AAO-PDP and AAO-C_{15}, we found that the thermal stability of both AAO-PDP and AAO-C_{15} decreased. The thermal stability of AAO-PDP decreased with the decrease in the confined space size, but the thermal stability of AAO-C_{15} hardly changed with the decrease of the confined space size. At the same time, we found that the thermal stability of PDP decreased more obviously than that of C_{15}, the thermal decomposition process of AAO-PDP showed one-step weight loss, while that of AAO-C_{15} showed two-step weight loss. Also, as shown in Figure 9e,f, at the heating rates of 15, 10, and 5 °C/min, the temperature differences corresponding to the maximum thermal decomposition rates of bulk PDP and 450 nm AAO-PDP were 62.2, 68.6, and 62.7 °C, respectively. The temperature differences at different heating rates were not much, so it can be proved that the thermal stability of the confined samples decreased due to the confinement effect, and the introduction of an end group made the confinement effect more obvious. The end groups with a phenol ring in the confined space were too bulky to be arranged regularly, resulting in the terminal defects and kinking defects in the molecular chain, which ultimately led to a decrease in the thermal stability of the PDP crystal.

2.5. Crystallinity Analysis. We used the total enthalpy method[62] to calculate the crystallinity X_c of the bulk samples and the confined samples.

$$X_c = \Delta H_m/(1 - w)\Delta H_f \quad (1)$$

where ΔH_m is the fusion enthalpy of the PDP and C_{15}, which were obtained from Figure 4. ΔH_f is the fusion enthalpy for 100% fully crystalline PDP and C_{15}. w is the mass percentage of AAO in the AAO-PDP and AAO-C_{15} samples, which was obtained by the TG results. To eliminate the influence of DSC heating rate, we replaced ΔH_f with equilibrium fusion enthalpy ΔH_m^0. The fusion enthalpies of bulk PDP and C_{15} were measured at the heating rates of 10, 5, 3, and 2 °C/min, respectively. Then, a straight line (Figure 10a) was drawn with the heating rates as the horizontal axis and the fusion enthalpies as the vertical axis. The equilibrium fusion enthalpies ΔH_m^0 were obtained when the heating rates were equal to zero, i.e., ΔH_m^0 of PDP was 173.88 J/g and ΔH_m^0 of C_{15} was 160.09 J/g. The ΔH_m and w of each sample at the heating rate of 10 °C/min were substituted into eq 1 to obtain the crystallinity of the bulk samples and the confined samples, the crystallinity of bulk PDP was 99.5%, and the crystallinity of bulk C_{15} was 97.0%, and the relationship between the crystallinity of the confined samples and the pore size is shown in Figure 10b. It can be seen from Figure 10b that under the same confined conditions, the crystallinity of PDP and C_{15} gradually decreased with the decrease in AAO pore size, and the crystallinity of C_{15} was higher than that of PDP. At the same time, by fitting X_c of the confined samples and the pore size d of AAO, we found that X_c of AAO-PDP had a good linear relationship with the pore size d, but X_c of AAO-C_{15} had a nonlinear relationship with the pore size d. These results indicated that AAO-PDP was more sensitive to the AAO pore size changes than AAO-C_{15}, further proving that the introduction of end groups made the confinement effect more obvious.

2.6. ATR-IR Analysis. Figure 11 shows the ATR-IR spectra of bulk PDP and 90 nm AAO-PDP. Compared with those of bulk PDP, some of the characteristic peaks of AAO-PDP shifted, and the intensity of some characteristic peaks decreased. For bulk PDP, the antisymmetric and symmetric stretching vibrations of $-CH_2$ appeared at 2915 and 2848 cm^{-1}, indicating that the alkyl chain was highly ordered and existed in an all-trans conformation.[63] The characteristic peaks at 1456 and 1360 cm^{-1} were the asymmetric and symmetric deformation vibrations of $-CH_3$.[61,63] After being confined, the antisymmetric stretching vibration of $-CH_2$ shifted from 2915 to 2928 cm^{-1}, the symmetric stretching vibration of $-CH_2$ shifted from 2848 to 2860 cm^{-1}, the asymmetric deformation vibration of $-CH_3$ shifted from 1456 to 1468 cm^{-1}, and the symmetric deformation vibration of $-CH_3$ shifted from 1360 to 1370 cm^{-1}. The intensity of the above characteristic peaks also decreased, of which the decrease of the intensity of the characteristic peak at 1468 cm^{-1} corresponded to the disappearance of the (00L) diffraction peak in WAXD. This proved that in the confined environment, the order of the alkyl chain decreased and the degree of chain distortion increased.

https://doi.org/10.1021/acsomega.1c02112
ACS Omega 2021, 6, 18235−18247

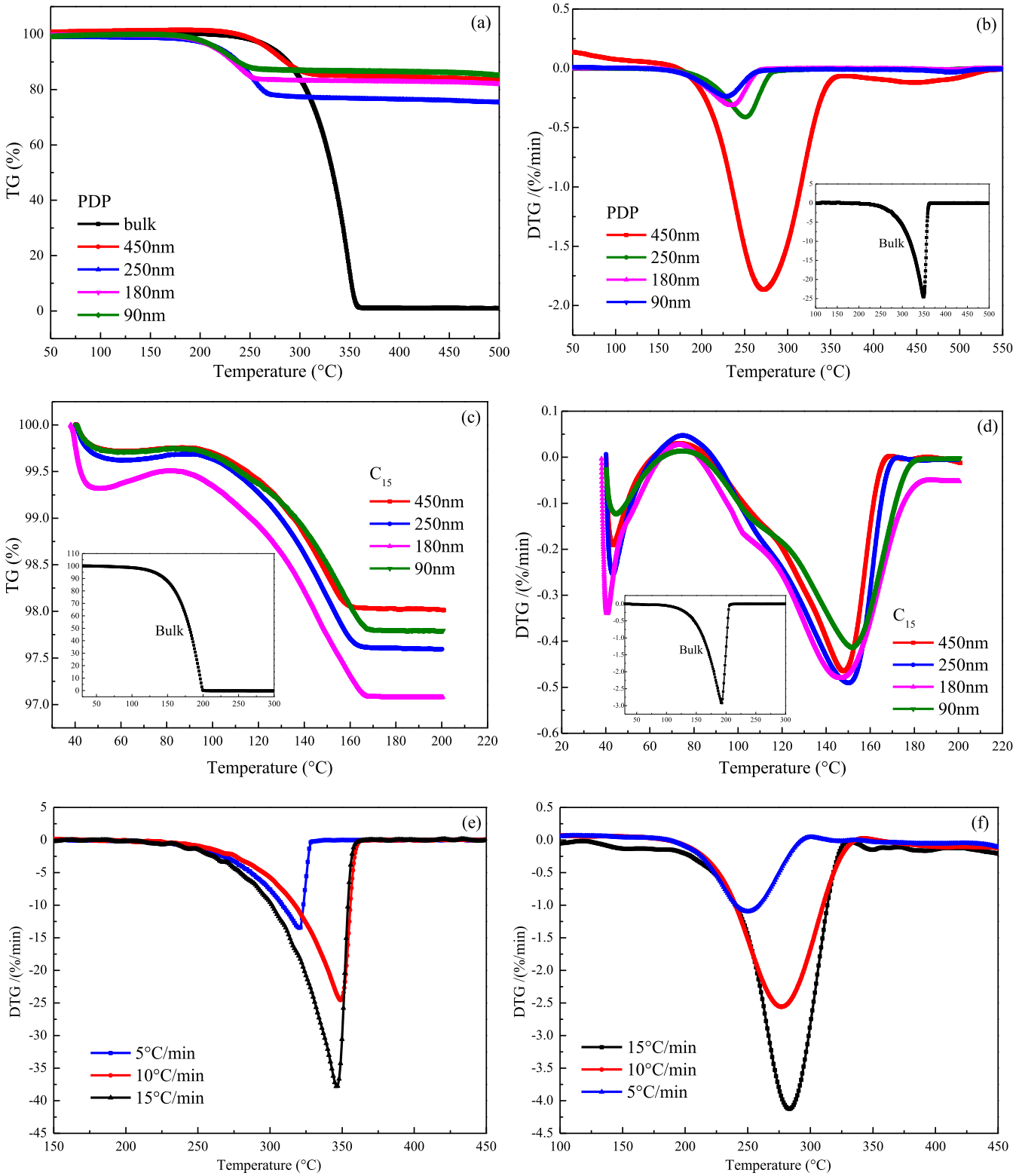

Figure 9. (a) Thermogravimetric (TG) and (b) derivative thermogravimetry (DTG) curves of bulk PDP and AAO-PDP samples. (c) TG and (d) DTG curves of bulk C_{15} and AAO-C_{15} samples. Heating rate: 10 °C/min. DTG curves of (e) bulk PDP and (f) 450 nm AAO-PDP at different heating rates.

3. EXPERIMENTAL SECTION

3.1. Materials and Sample Preparation. 3-Pentadecylphenol (PDP, $C_{21}H_{36}O$, M_w = 304.5 g/mol) was produced by Tokyo Chemical Industry Co., Ltd. *n*-Pentadecane ($C_{15}H_{32}$, M_w = 212.41 g/mol, purity ≥99.8%) and cyclohexane (C_6H_{12}, M_w = 84.16 g/mol, purity ≥99.5%) were purchased from Shanghai Aladdin Biochemical Technology Co., Ltd. The AAO templates with a thickness of about 60 μm and pore diameters of 90, 180, 250, and 450 nm were bought from Hefei Pu-Yuan Nano Technology Limited Company. Before use, the AAO

https://doi.org/10.1021/acsomega.1c02112
ACS Omega 2021, 6, 18235−18247

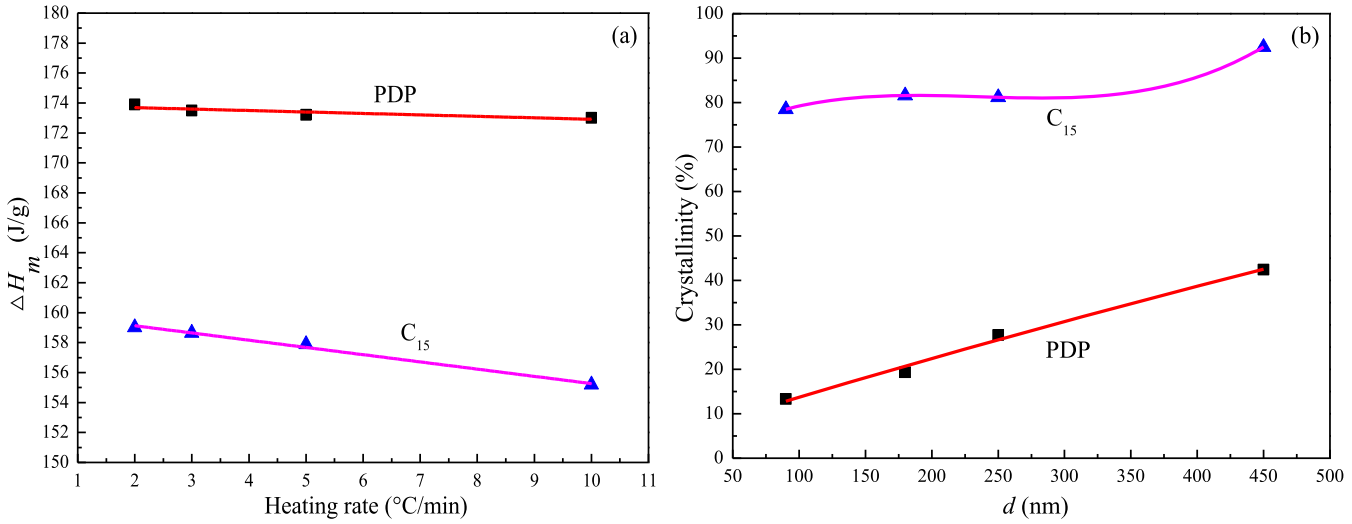

Figure 10. (a) Relationship between heating rate and ΔH_m. (b) Relationship between AAO pore size d and the crystallinity of confined samples.

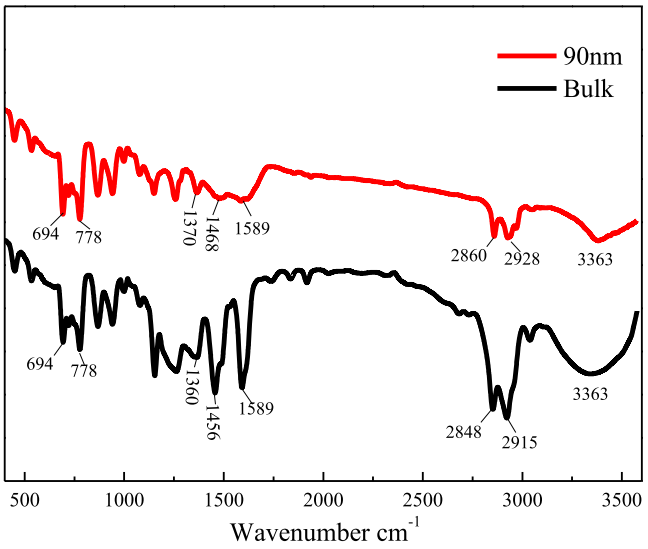

Figure 11. ATR-IR spectra of bulk PDP and 90 nm AAO-PDP.

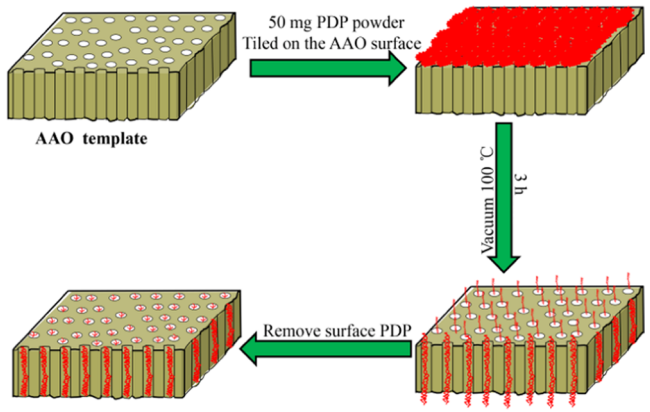

Figure 12. Brief preparation process of the AAO-PDP samples.

templates were first cleaned with ethanol and water to eliminate the influence of impurities and then dried in a vacuum oven at 100 °C for 12 h. The PDP powder was dried in a vacuum at 40 °C for 12 h before use. PDP was infiltrated into AAO pores with different pore sizes (90, 180, 250, 450 nm) by the melt infiltration method, and PDP confined samples (90, 180, 250, 450 nm AAO-PDP) were thus obtained. As shown in Figure 12, a thin layer of PDP powder with a mass of 50 mg was evenly tiled on the surface of the AAO template and then annealed at 100 °C for 3 h in a vacuum oven. After melt infiltration, to remove excess PDP from the surface of the AAO templates, four steps were taken. First, excessive molten PDP on the surface of the templates was cleaned with lens paper at a temperature above the melting temperature of bulk PDP. Second, excess PDP power on the surface of the AAO template was scraped with a sharp blade below the crystallization temperature of bulk PDP. Third, the samples were further polished by fine-grade sandpaper at room temperature. Finally, the surface of the templates was scrubbed with a lens paper, which was moistened with cyclohexane, and then samples were placed in a vacuum for several hours to ensure that cyclohexane was fully volatilized. The preparation of *n*-pentadecane confined samples (AAO-C_{15}) was similar to that of the PDP confined samples.

3.2. Characterization. A Zeiss Merlin Compact scanning electron microscope (SEM), operated at 5 kV, was utilized to examine the surface and cross-sectional morphology of the AAO-PDP samples. WAXD measurements were performed on a D8 Advance A25 diffractometer (AXS, Germany) in the 2θ range from 3 to 60° at a scanning rate of 2 °/min at room temperature. The WAXD data were collected using Cu Kα radiation (λ = 0.154 nm). The voltage and current were set at 40 kV and 40 mA, respectively. In situ WAXS were performed on a Rigaku Smartlab diffractometer at heating and cooling rates of 2 °C/min. First, the samples were heated from 0 to 60 °C and kept at 60 °C for 3 min. Then, the samples were cooled from 60 to 0 °C. Finally, the samples were heated from 0 to 60 °C. The samples were scanned during the heating and cooling processes and equilibrated at each test point for 5 min before scanning. Thermal analysis was conducted with a differential scanning calorimeter (DSC Q20, TA) under the nitrogen atmosphere with a flow rate of 50 mL/min. Before the measurement, the temperature and heat flow at different heating rates were carefully calibrated with indium. Samples of 4−6 mg were weighed accurately and encapsulated in aluminum pans. First, the samples were heated from 20 to 100 °C at the heating rate of 10 °C/min and held for 5 min to

https://doi.org/10.1021/acsomega.1c02112
ACS Omega 2021, 6, 18235−18247

eliminate the thermal history. Then, the samples were cooled to −20 °C at the cooling rate of 10 °C/min and heated back to 100 °C at the heating rate of 10 °C/min. Finally, the cooling and heating rates were changed to 5, 3, 2, and 1 °C/min, and the above operations were repeated. The TG analysis of the bulk and AAO-PDP samples were accomplished on a thermal gravimetric analyzer (NETZSCH STA 449F3) under nitrogen purge. The samples were heated from 30 to 600 °C at the heating rate of 5, 10, and 15 °C/min.

4. CONCLUSIONS

In summary, our study reported the crystallization and melting behaviors of bulk PDP and AAO-PDP samples. The space−time equivalence was well reflected in the PDP crystallization processes; in other words, AAO-PDP exhibited thorough solid−solid phase transitions at any selected cooling rates, while bulk PDP exhibited incomplete solid−solid phase transitions only at low cooling rates. Thus, in the process of research or production of phase change materials, the solid−solid phase transition can be achieved by reducing the cooling rate or confining the materials in the nanospace. Bulk PDP exhibited overlapping double melting peaks and cold crystallization peaks, indicating that the solid−solid phase transition of bulk PDP during the corresponding crystallization process was not thorough enough, and there were two crystal types when the crystallization was completed. For the AAO-PDP samples, only one single melting peak was observed at different heating rates, but bulk PDP showed partially overlapping double melting peaks, which is very common in the melting processes of semicrystalline polymers. This proved that the crystallization of PDP is more similar to that of semicrystalline polymers; so, the simulation of confined crystallization of semicrystalline polymers by PDP is more realistic than that of *n*-alkanes. In a confined environment, the arrangement of the bulky phenol rings in the nanopore was strongly confined, which made the movement of the alkyl chain lose part of the "independent consciousness", resulting in the disappearance of the surface frozen monolayer and resulting in the change of double melting peaks to a single melting peak. Under the same confined conditions, the crystallinity of PDP and C_{15} gradually decreased with the decrease of the AAO pore size, but AAO-PDP was more sensitive to AAO pore size changes than AAO-C_{15}, which proved the introduction of end groups made the confinement effect more obvious. Thus, this showed that we can adjust the crystallization behaviors by introducing side chains or end groups within a confined space.

AUTHOR INFORMATION

Corresponding Authors

Min Yao − *State Key Laboratory of High-Efficiency Coal Utilization and Green Chemical Engineering, Ningxia University, Yinchuan 750021, China; Ningxia Baofeng Energy Group, Yinchuan 750001, China*; Email: ndglym@163.com

Faliang Luo − *State Key Laboratory of High-Efficiency Coal Utilization and Green Chemical Engineering, Ningxia University, Yinchuan 750021, China*; orcid.org/0000-0002-0077-3287; Email: flluo@iccas.ac.cn

Authors

Yongdong Liu − *State Key Laboratory of High-Efficiency Coal Utilization and Green Chemical Engineering, Ningxia University, Yinchuan 750021, China*

Yonghong Wu − *State Key Laboratory of High-Efficiency Coal Utilization and Green Chemical Engineering, Ningxia University, Yinchuan 750021, China*

Jianqi Yao − *State Key Laboratory of High-Efficiency Coal Utilization and Green Chemical Engineering, Ningxia University, Yinchuan 750021, China*

Jiajie Yin − *State Key Laboratory of High-Efficiency Coal Utilization and Green Chemical Engineering, Ningxia University, Yinchuan 750021, China*

Jing Lu − *State Key Laboratory of High-Efficiency Coal Utilization and Green Chemical Engineering, Ningxia University, Yinchuan 750021, China*

Jie Mao − *State Key Laboratory of High-Efficiency Coal Utilization and Green Chemical Engineering, Ningxia University, Yinchuan 750021, China*

Complete contact information is available at: https://pubs.acs.org/10.1021/acsomega.1c02112

Author Contributions

Y.L. performed the experiments, analyzed the data, and wrote the manuscript. Y.W., J.Q.Y., J.J.Y., and J.L. assisted in sample characterization and data analysis. J.M. revised the manuscript.

Notes

The authors declare no competing financial interest.

ACKNOWLEDGMENTS

The authors thank The East-West Cooperation Project of Ningxia Key R&D Plan (Grant No. 2019BFH02018) and the First-Class Discipline Construction (Chemical Engineering and Technology) of Ningxia University (Grant No. NXYLX-K2017A04) for the financial support.

REFERENCES

(1) Liu, G. M.; Shi, G. Y.; Wang, D. J. Research progress on polymer crystallization confined within nanoporous AAO templates. *Acta Polym. Sin.* **2020**, *51*, 501−516.

(2) Vanroy, B.; Wübbenhorst, M.; Napolitano, S. Crystallization of thin polymer layers confined between two adsorbing walls. *ACS Macro Lett.* **2013**, *2*, 168−172.

(3) Nanjundiah, K.; Kurian, A.; Kaur, S.; Singla, S.; Dhinojwala, A. Crystallinelike ordering of confined liquids at the moving contact line. *Phys. Rev. Lett.* **2019**, *122*, No. 128004.

(4) Nakagawa, S.; Kadena, K. I.; Ishizone, T.; Nojima, S.; Shimizu, T.; Yamaguchi, K.; Nakahama, S. Crystallization behavior and crystal orientation of Poly(ε-caprolactone) homopolymers confined in nanocylinders: Effects of nanocylinder dimension. *Macromolecules* **2012**, *45*, 1892−1900.

(5) Guan, Y.; Liu, G. M.; Ding, G. Q.; Yang, T. Y.; Müller, A. J.; Wang, D. J. Enhanced crystallization from the glassy state of Poly(l-lactic acid) confined in anodic alumina oxide nanopores. *Macromolecules* **2015**, *48*, 2526−2533.

(6) Su, C.; Chen, Y.; Shi, G. Y.; Tang, L.; Liu, G. M.; Müller, A. J.; Wang, D. J. Crystallization kinetics of Poly(ethylene oxide) under confinement in nanoporous alumina studied by in situ X-ray scattering and simulation. *Langmuir* **2019**, *35*, 11799−11808.

(7) Su, C.; Shi, G. Y.; Li, X. L.; Zhang, X. Q.; Müller, A. J.; Wang, D. J.; Liu, G. M. Uniaxial and mixed orientations of Poly(ethylene oxide) in nanoporous alumina studied by X-ray pole figure analysis. *Macromolecules* **2018**, *51*, 9484−9493.

(8) Shi, G. Y.; Liu, G. M.; Su, C.; Chen, H. M.; Chen, Y.; Su, Y. L.; Müller, A. J.; Wang, D. J. Reexamining the crystallization of Poly(ε-

caprolactone) and isotactic polypropylene under hard confinement: Nucleation and orientation. *Macromolecules* **2017**, *50*, 9015−9023.
(9) Gao, X.; Fu, D. S.; Su, Y. L.; Zhou, Y.; Wang, D. J. Phase transition behavior of a series of even *n*-alkane C_n/C_{n+2} mixtures confined in microcapsules: From total miscibility to phase separation determined by confinement geometry and repulsion energy. *J. Phys. Chem. B* **2013**, *117*, 13914−13921.
(10) Fu, D. S.; Liu, Y. F.; Gao, X.; Su, Y. L.; Liu, G. M. Binary *n*-alkane mixtures from total miscibility to phase separation in microcapsules: Enrichment of shorter component in surface freezing and enhanced stability of rotator phases. *J. Phys. Chem. B* **2012**, *116*, 3099−105.
(11) Xie, B. Q.; Liu, G. M.; Jiang, S. C.; Zhao, Y.; Wang, D. J. Crystallization behaviors of n-octadecane in confined space: crossover of rotator phase from transient to metastable induced by surface freezing. *J. Phys. Chem. B* **2008**, *112*, 13310−13315.
(12) Taden, A.; Landfester, K. Crystallization of Poly(ethylene oxide) Confined in Miniemulsion Droplets. *Macromolecules* **2003**, *36*, 4037−4041.
(13) Alcoutlabi, M.; Mckenna, G. B. Effects of confinement on material behaviour at the nanometre size scale. *J. Phys.: Condens. Matter* **2005**, *17*, R461−R524.
(14) Liu, C. L.; Chen, H. L. Crystal orientation of PEO confined within the nanorod templated by AAO nanochannels. *Soft Matter* **2018**, *14*, 5461−5468.
(15) Su, C.; Shi, G. Y.; Wang, D. J.; Liu, G. M. A model for the crystal orientation of polymers confined in 1D nanocylinders. *Acta Polym. Sin.* **2019**, *50*, 281−290.
(16) Safari, M.; Maiz, J.; Shi, G. Y.; Juanes, D.; Liu, G. M.; Wang, D. J.; Mijangos, C.; Alegría, A.; Müller, A. J. How confinement affects the nucleation, crystallization, and dielectric relaxation of Poly(butylene succinate) and Poly(butylene adipate) infiltrated within nanoporous alumina templates. *Langmuir* **2019**, *35*, 15168−15179.
(17) Nikam, P. N.; Deshpande, V. D. Isothermal crystallization kinetics of PET/alumina nanocomposites using distinct macrokinetic models. *J. Therm. Anal. Calorim.* **2019**, *138*, 1049−1067.
(18) Guan, Y.; Liu, G. M.; Gao, P. Y.; Li, L.; Ding, G. Q.; Wang, D. J. Manipulating crystal orientation of poly(ethylene oxide) by nanopores. *ACS Macro Lett.* **2013**, *2*, 181−184.
(19) Michell, R. M.; Lorenzo, A. T.; Müller, A. J.; Lin, M. C.; Chen, H. L.; Blaszczyk-Lezak, I.; Martín, J.; Mijangos, C. The crystallization of confined polymers and block copolymers infiltrated within alumina nanotube templates. *Macromolecules* **2012**, *45*, 1517−1528.
(20) Michell, R. M.; Müller, A. J. Confined crystallization of polymeric materials. *Prog. Polym. Sci.* **2016**, *54*−*55*, 183−213.
(21) Martín, J.; Maiz, J.; Sacristan, J.; Mijangos, C. Tailored polymer-based nanorods and nanotubes by "template synthesis": From preparation to applications. *Polymer* **2012**, *53*, 1149−1166.
(22) Mijangos, C.; Hernández, R.; Martin, J. A review on the progress of polymer nanostructures with modulated morphologies and properties, using nanoporous AAO templates. *Prog. Polym. Sci.* **2016**, *54*−*55*, 148−182.
(23) Masuda, H.; Fukuda, K. Ordered metal nanohole arrays made by a two-step replication of honeycomb structures of anodic alumina. *Science* **1995**, *268*, 1466−1468.
(24) Wu, H.; Higaki, Y.; Takahara, A. Molecular self-assembly of one-dimensional polymer nanostructures in nanopores of anodic alumina oxide templates. *Prog. Polym. Sci.* **2018**, *77*, 95−117.
(25) Michell, R. M.; Blaszczyk-Lezak, I.; Mijangos, C.; Müller, A. J. Confinement effects on polymer crystallization: From droplets to alumina nanopores. *Polymer* **2013**, *54*, 4059−4077.
(26) Shi, G. Y.; Wang, Z. F.; Wang, M.; Liu, G. M.; Wang, D. J. Crystallization, orientation, and solid−solid crystal transition of polybutene-1 confined within nanoporous alumina. *Macromolecules* **2020**, *53*, 6510−6518.
(27) Fu, D. S.; Su, Y. L.; Gao, X.; Liu, Y. F.; Wang, D. J. Confined crystallization of n-hexadecane located inside microcapsules or outside submicrometer silica nanospheres: A comparison study. *J. Phys. Chem. B* **2013**, *117*, 6323−6329.
(28) Uhlmann, D. R.; Kritchevsky, G.; Straff, R.; Scherer, G. Crystal nucleation in normal alkane liquid. *J. Chem. Phys.* **1975**, *62*, 4896−4903.
(29) Taggart, A. M.; Voogt, F.; Clydesdale, G.; Roberts, K. J. An examination of the nucleation kinetics of *n*-alkanes in the homologous series $C_{13}H_{28}$ to $C_{32}H_{66}$, and their relationship to structural type, associated with crystallization from stagnant melts. *Langmuir* **1996**, *12*, 5722−5728.
(30) Montenegro, R.; Landfester, K. Metastable and stable morphologies during crystallization of alkanes in miniemulsion droplets. *Langmuir* **2003**, *19*, 5996−6003.
(31) Xia, G.; Su, Y. L.; Xie, B. Q.; Fu, D. S.; Wang, D. J. Progress in studies of confined crystallization of long-chain *n*-alkanes. *Acta Polym. Sin.* **2014**, *14*, 22−30.
(32) Konuklu, Y.; Ersoy, O.; Erzin, F. Development of pentadecane/diatomite and pentadecane/sepiolite nanocomposites fabricated by different compounding methods for thermal energy storage. *Int. J. Energy Res.* **2019**, *43*, 6510−6520.
(33) Konuklu, Y.; Erzin, F. Preparation of pentadecane/poly-(melamine-urea-formaldehyde) microcapsules for thermal energy storage applications. *Int. J. Energy Res.* **2019**, *43*, 6322−6326.
(34) Gao, X.; Huber, P.; Su, Y. L.; Zhao, W. W.; Wang, D. J. Two-Step freezing in alkane monolayers on colloidal silica nanoparticles: From a stretched-liquid to an interface-frozen state. *J. Phys. Chem. B* **2016**, *120*, 7522−7528.
(35) Tubbs, K. W.; Nguyen, V. T.; Adalsteinsson, T. Phase transitions of n-hexadecane in nanoencapsulated binary solutions of n-hexadecane and 1-octanol. *J. Phys. Chem. B* **2012**, *116*, 3954−3960.
(36) Fu, D. S.; Su, Y. L.; Xie, B. Q.; Zhu, H. J.; Liu, G. M.; Wang, D. J. Phase change materials of *n*-alkane-containing microcapsules: Observation of coexistence of ordered and rotator phases. *Phys. Chem. Chem. Phys.* **2011**, *13*, 2021−2026.
(37) Huber, P.; Soprunyuk, V. P.; Knorr, K. Structural transformations of even-numbered *n*-alkanes confined in mesopores. *Phys. Rev. E.* **2006**, *74*, 1539−3755.
(38) Ueno, S.; Hamada, Y.; Sato, K. Controlling polymorphic crystallization of *n*-alkane crystals in emulsion droplets through interfacial heterogeneous nucleation. *Cryst. Growth. Des.* **2003**, *3*, 935−939.
(39) Sirota, E. B.; Herhold, A. B. Transient rotator phase induced nucleation in *n*-alkane melts. *Polymer* **2000**, *41*, 8781−8789.
(40) Kraack, H.; Sirota, E. B.; Deutsch, M. Measurements of homogeneous nucleation in normal-alkanes. *J. Chem. Phys.* **2000**, *112*, 6873−6885.
(41) Zhang, F. B.; Xie, X. M.; Yuan, J. Y.; Yuan, W. Z.; Yan, Q. Influence of end group on the banded structure of PLLA spherulites. *Acta Polym. Sin.* **2011**, *11*, 488−493.
(42) Li, X.; Dong, X. L.; Zhou, J. L.; Bao, J. N.; Chen, S. C.; Lu, W. Y.; Zhang, X. M.; Chen, W. X. Confined crystallization and melting behaviors of poly(ethylene glycol) end-functionalized by hydrogen bonding groups: Effect ofcontents for functional units. *Polym. Cryst.* **2020**, *3*, No. e10158.
(43) Cheng, S. Z. D.; Wu, S. S.; Chen, J.; Zhuo, Q.; Quirk, R. P.; von Meerwall, E. D.; Hsiao, B. S.; Habenschuss, A.; Zschack, P. R. Isothermal thickening and thinning processes in low-molecular-weight Poly(ethylene oxide) fractions crystallized from the melt. 4. End-group dependence. *Macromolecules* **1993**, *26*, 5105−5117.
(44) Huang, X. D.; Goh, S. H. Crystallization of C60-end-capped poly(ethylene oxide)s. *Macromolecules* **2001**, *34*, 3302−3307.
(45) Qin, Y. S.; Zhu, Y. L.; Luo, X.; Liang, S.; Wang, J. H.; Zhang, L. End group modification of polyethylene glycol (PEG): A novel method to mitigate the supercooling of PEG as phase change material. *Int. J. Energy Res.* **2019**, *43*, 1000−1011.
(46) Krutyeva, M.; Brás, A.; Antonius, W.; Hvelmann, C. H.; Richter, D. Association behavior, diffusion, and viscosity of end-functionalized supramolecular Poly(ethylene glycol) in the melt state. *Macromolecules* **2015**, *48*, 8933−8946.

https://doi.org/10.1021/acsomega.1c02112
ACS Omega 2021, 6, 18235−18247

(47) González-Fernández, D.; Torneiro, M.; Lazzari, M. Some guidelines for the synthesis and melting characterization of azide poly (ethylene glycol) derivatives. *Polymers* **2020**, *12*, No. 1269.
(48) Cieślik-Boczula, K.; Küpcü, S.; Rünzler, D.; Koll, A.; Köhler, G. Effects of the phenolic lipid 3-pentadecylphenol on phospholipid bilayer organization. *J. Mol. Struct.* **2008**, *919*, 373−380.
(49) Jiang, K.; Su, Y. L.; Xie, B. Q.; Meng, Y. F.; Wang, D. J. Suppression of the phase separation in binary *n*-alkane solid solutions by geometrical confinement. *J. Phys. Chem. B* **2009**, *113*, 3269−3272.
(50) Rajabalee, F.; Metivaud, V.; Mondieig, D. New insights on the crystalline forms in binary systems of *n*-alkanes: Characterization of the solid ordered phases in the phase diagram tricosane + pentacosane. *J. Mater. Res.* **1999**, *14*, 2644−2654.
(51) Espeau, P.; Rajabalee, F.; Haget, Y. Binary Phase Diagram with Non Isomorphous *n*-alkanes: $C_{12}H_{26}$-$C_{15}H_{32}$. Implication of the rotator phase R, in the melting behaviour of odd-even and even-odd phase diagrams. *Mol. Cryst. Liq. Cryst. Sci. Technol., Sect. A* **1998**, *323*, 145−153.
(52) Wu, X. Z.; Ocko, B. M.; Sirota, E. B.; Sinha, S. K.; Deutsch, M.; Cao, B. H.; Kim, M. W. Surface tension measurements of surface freezing in liquid normal alkanes. *Science* **1993**, *261*, 1018−1021.
(53) Blaszczyk-Lezak, I.; Hernández, M.; Mijangos, C. One dimensional PMMA nanofibers from AAO templates. Evidence of confinement effects by dielectric and raman analysis. *Macromolecules* **2013**, *46*, 4995−5002.
(54) Wang, H. X.; Chang, T. X.; Li, X. H.; Zhang, W. D.; Hu, Z. J.; Jonas, A. M. Scaled down glass transition temperature in confined polymer nanofibers. *Nanoscale* **2016**, *8*, 14950−14955.
(55) Sun, X. L.; Luo, F. L.; Yan, D. G. The preparation of chain branching PLLA by intermolecular hydrogen bonding with 3-Pentadecylphenol and its crystallization, relaxation behavior and thermal stability. *J. Polym. Res.* **2019**, *26*, No. 81.
(56) Song, P.; Chen, G. Y.; Wei, Z. Y.; Zhang, W. X.; Liang, J. C. Calorimetric analysis of the multiple melting behavior of melt-crystallized poly(l-lactic acid) with a low optical purity. *J. Therm. Anal. Calorim.* **2013**, *111*, 1507−1514.
(57) Shan, G. F.; Wei, Y.; Tang, X. G.; Yang, M. B.; Xie, B. H.; Qiang, F.; Mai, Y. W. Multiple melting behaviour of annealed crystalline polymers. *Polym. Test.* **2010**, *29*, 273−280.
(58) Yasuniwa, M.; Tsubakihara, S.; Satou, T.; Iura, K. Multiple melting behavior of Poly(butylene succinate). II. Thermal analysis of isothermal crystallization and melting process. *J. Polym. Sci., Part B: Polym. Phys.* **2005**, *43*, 2039−2047.
(59) Vélez, C.; Ortiz de Zárate, J. M.; Khayet, M. Thermal properties of n-pentadecane, n-heptadecane and n-nonadecane in the solid/liquid phase change region. *Int. J. Therm. Sci.* **2015**, *94*, 139−146.
(60) Alvarado, J. L.; Marsh, C.; Sohn, C.; Vilceus, M.; Hock, V.; Phetteplace, G.; Newell, T. Characterization of supercooling suppression of microencapsulated phase change material by using DSC. *J. Therm. Anal. Calorim.* **2006**, *86*, 505−509.
(61) Cieślik-Boczula, K.; Koll, A. The effect of 3-pentadecylphenol on DPPC bilayers ATR-IR and ^{31}P NMR studies. *J. Biophys. Chem.* **2008**, *140*, 51−56.
(62) Blundell, D. J.; Beckett, D. R.; Willcocks, P. H. Routine crystallinity measurements of polymers by DSC. *Polymer* **1981**, *22*, 704−707.
(63) Eichhorn, K. J.; Fahmi, A.; Adam, G.; Stamm, M. Temperature-dependent FTIR spectroscopic studies of hydrogen bonding of the copolymer Poly(styrene-b-4-vinylpyridine) with pentadecylphenol. *J. Mol. Struct.* **2003**, *661−662*, 161−170.

https://doi.org/10.1021/acsomega.1c02112
ACS Omega 2021, 6, 18235−18247